DOI: 10.13009/EUCASS2019-300

DOI: ADD DOINUMBER HERE

Numerical investigation of jet-wake interaction for a generic space launcher with a dual-bell nozzle

S. Loosen[⋆†], *M. Meinke*[⋆,⋆⋆] *and W. Schröder*[⋆,⋆⋆]

[⋆] *Institute of Aerodynamics and Chair of Fluid Mechanics*
RWTH Aachen University, Wüllnerstraße 5a, 52062 Aachen, Germany
[⋆⋆] *JARA Center for Simulation and Data Science*
RWTH Aachen University, Seffenter Weg 23, 52074 Aachen, Germany
e-mail: s.loosen@aia.rwth-aachen.de
[†]Corresponding author

Abstract

The turbulent wake of a generic axisymmetric space launcher equipped with a dual-bell nozzle is numerically investigated to examine the influence of the dual-bell nozzle jet on the wake flow. The simulation is performed at transonic freestream condition, i.e., freestream Mach number $Ma_\infty = 0.8$ and freestream Reynolds number based on the launcher diameter $Re_D = 4.3 \cdot 10^5$, with the dual-bell nozzle operating in sea-level mode. A zonal RANS/LES approach is used and the time-resolved flow field data is analyzed by classical spectral analysis and dynamic mode decomposition (DMD). The overall flow topology of the recirculation region downstream of the base and the pressure loads on the outer nozzle fairing are only slightly affected by the modified nozzle shape. However, the changed nozzle flow topology characterized by the flow separation at the nozzle contour inflection leads to a backflow region and an entrainment of the outer flow into the nozzle extension which results in increased fluctuation levels inside the nozzle. The pressure fluctuations on the outer nozzle surface are investigated using spectral analysis revealing two characteristic frequencies at $S r_D \approx 0.04$ and $S r_D \approx 0.2$. It is shown by two-point correlation that the buffet loads at $S r_D \approx 0.2$ are caused by an antisymmetric mode in the circumferential direction containing more than 75% of the fluctuating energy. By performing a DMD analysis of the wake flow it is shown that the buffet loads originate from an antisymmetric vortex shedding. Additionally, an antisymmetric growing and contracting of the separation bubble at $S r_D \approx 0.04$ is revealed explaining the low frequency pressure loads. The investigated dual-bell nozzle configuration features a flow topology and dynamics similar to configurations with conventional nozzles indicating that in the present flow parameter regime and operation mode the impact of the dual-bell nozzle is insignificant.

1. Introduction

The main stage engine of a classical parallel staging space launcher like the European Ariane 5 operates in a broad altitude range, i.e., from sea-level up to almost vacuum conditions. To prevent flow separation at sea-level mode which would lead to strong side loads, the maximum area ratio of the nozzle is limited. Since the ambient pressure decreases with increasing altitude, a larger area ratio without flow separation would be possible at altitude mode leading to a higher specific impulse and thus, to an increased payload mass. An advanced propulsion concept which avoids this constraint is altitude adaptive nozzles like the dual-bell nozzle with a larger feasible area ratio at altitude conditions. The dual-bell nozzle consists of a conventional bell nozzle, i.e., the base nozzle, and an extension nozzle. The combination of both nozzles results in an abrupt contour inflection. Depending on the nozzle pressure ratio (NPR), which is the ratio of the chamber pressure to the ambient pressure, the dual-bell nozzle features two operating conditions which are shown in Fig. 1. At sea-level mode when NPR is smaller than the transition nozzle pressure ratio (NPR_{tr}), the flow is attached in the base nozzle and a controlled and symmetric flow separation takes place at the abrupt inflection preventing any side loads. At a certain flight altitude, when NPR is greater than NPR_{tr}, the separation point shifts from the inflection to the nozzle exit leading to a symmetric attached flow in the complete nozzle. Due to the larger area ratio, the expansion of the nozzle flow is increased leading to an improved performance at altitude mode compared to classical rocket engines. The dual-bell flow behavior, e.g., the transition behavior, the arising side loads, and the payload gain, has

DOI: 10.13009/EUCASS2019-300

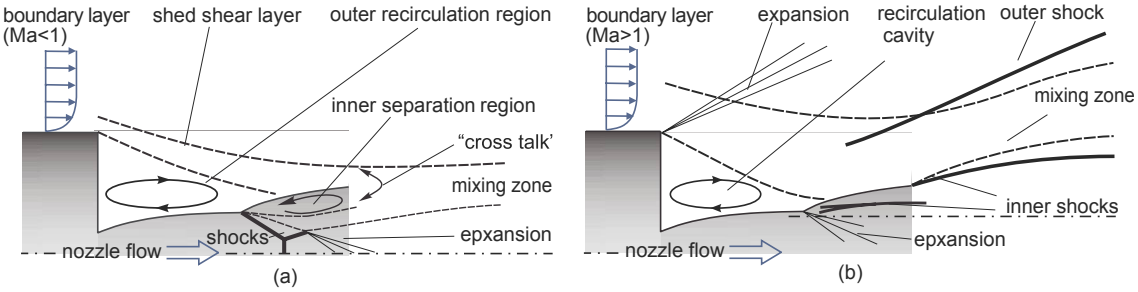

Figure 1: Schematic of the interaction of the wake flow with a dual-bell nozzle operating at sea-level mode (left) and altitude mode (right).

experimentally, e.g., by Stark et al.[26] and Proshchanka et al.[18] , and numerically, e.g., by Martelli et al.[17] and Schneider and Genin[23] , been investigated proving the functionality of the adaptive nozzle concept. More recently, Loosen et al.[16] , investigated the aerodynamic integration of the dual-bell nozzle into the launcher's architecture and the influence of the outer flow onto the dual-bell nozzle flow for a generic planar space launcher configuration. However, the effect of a dual-bell nozzle on the wake of an axisymmetric free flight configuration has not been investigated, yet.

The wake flow is characterized by the separation of the incoming boundary layer at the base shoulder and its subsequent reattachment on the nozzle leading to the formation of a highly dynamic recirculation region. The turbulent wake flow behind the base exhibits many similarities with the flow past a planar backward-facing step (BFS) extensively studied experimentally, e.g., by Bradshaw and Wong[3] , Eaton and Johnston[9] , Driver et al.[8] , and numerically, e.g., by Friedrich and Arnal[11] , Silveira Neto et al.[25] , Le et al.[14] , and Lee and Sung[15] . In all these investigations, a variation of the instantaneous impingement location of the separated shear layer by about two step heights around the mean reattachment position is reported. In addition, two basic modes of characteristic frequencies were detected in nearly all of these studies. The low frequency mode at a Strouhal number of $Sr_h = 0.012 - 0.014$ based on the step height and the freestream velocity reflects an overall increase and decrease of the separation bubble or shear-layer "flapping" as it is commonly called in the literature. The aforementioned time-dependent variation of the instantaneous reattachment position can be attributed to this "flapping" motion. The higher frequency mode at $Sr_h = 0.065 - 0.08$ is attributed to a Kelvin-Helmholtz like vortex-shedding instability. The studies on planar BFS flows are mainly limited to two-dimensional observations or spanwise averaged flow properties. More recently, Statnikov et al.[27] , Scharnowski et al.[21] , and Bolgar et al.[1] analyzed the three-dimensional wake of a generic planar launcher consisting of a BFS with a long forebody. It was shown that the reattachment position varies over time not only in the streamwise but also in the spanwise direction leading to a formation of wedge-shaped reattachment regions. Using a dynamic mode decomposition (DMD) analysis[27] , this variation in the reattachment process can be traced back to a coherent longitudinal cross-pumping motion of the recirculation bubble at $Sr_D = 0.04$ ($Sr_h = 0.012$) and a cross-flapping motion of the shear layer at $Sr_D = 0.23$ ($Sr_h = 0.07$), where D is the "thickness" of the launcher.

Besides the presented studies on planar configurations, many experimental and numerical investigations on a large range of different axisymmetric more realistic space launcher configurations ranging from axisymmetric backward-facing steps up to scaled real launchers have been conducted, e.g. Deprés et al.[7] , Deck and Thorigny[6] , Schrijer et al.[24] , and Statnikov et al.[28,29] . Schrijer et al. used POD to analyze a time series of snapshots of 2D-PIV measurements and detected two dominant wake modes containing the majority of the turbulent kinetic energy. The first low frequency mode captures an oscillating growing and shrinking of the separation zone, most probably being related to the shear-layer "flapping" detected in the planar BFS flows or to the more recently observed three-dimensional cross-pumping motion by Statnikov et al.[27] in a planar space launcher configuration. The second higher frequency mode describes an undulating motion of the shear layer coinciding with the vortex-shedding of the BFS flow (Le et al.[14]) and the cross-flapping motion of the planar space launcher (Statnikov et al.[27]) . Statnikov et al.[27] performed a dynamic mode decomposition of the flow around a generic Ariane 5-like configuration to analyze the coherent structures being responsible for side forces occurring for axisymmetric configurations. Three distinct modes at $Sr_D \approx 0.1; 0.2; 0.35$ which could generate buffet were detected. The low frequency mode describes a longitudinal cross-pumping motion of the separation region, the second mode is associated with a cross-flapping motion of the shear layer caused by antisymmetric vortex shedding, and the high frequency mode represents a swinging motion of the shear layer.

In the present study, an axisymmetric generic space launcher equipped with a dual-bell nozzle will be investigated at transonic flow conditions to determine the influence of the new propulsion concept onto the intricate wake-nozzle flow interaction. The analysis will be performed for the dual-bell nozzle operating at sea-level mode, i.e., with the inner separation at the contour inflection. Besides classical statistical analyses such as mean and root-mean-square

DOI: 10.13009/EUCASS2019-300

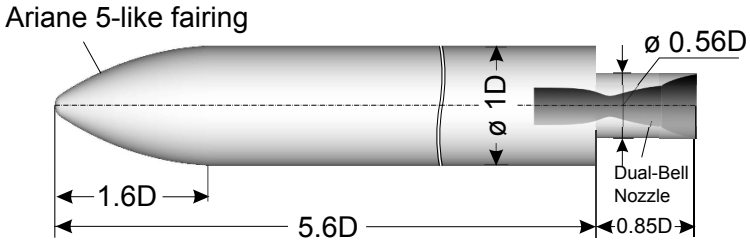

Figure 2: Geometry parameters of the investigated generic axisymmetric transonic configuration.

distributions and spectral analyses, DMD is used to analyze the wake flow. The investigated flow field is characterized by a superposition of flow structures exhibiting various time and length scales. Therefore, it is challenging to identify the flow mechanisms which are responsible for the dynamic loads acting onto the nozzle wall. The DMD method, which belongs to a class of data-driven modal decomposition techniques, enables to isolate spatial modes such that insight into the underlying flow mechanisms is obtained.

The paper is organized as follows. In Sec. 2, the investigated geometry and the flow parameters are presented. The zonal RANS/LES method, the computational grids, and the DMD algorithm are briefly described. In Sec. 3, the results of the performed simulations are discussed. First, the wake flow topology including the jet is described. Then, the pressure loads on the nozzle wall are investigated by spectral analysis followed by a modal analysis of the wake flow by DMD. Finally, conclusions are drawn in Sec. 4.

2. Computational Approach

In this section, the geometry and flow parameters, the zonal RANS/LES method, the computational grids, and the DMD algorithm are discussed.

2.1 Geometry and flow conditions

The aerodynamic integration of the dual-bell nozzle into the space launcher and the influence of the new propulsion concept onto the intricate wake flow is investigated for an axisymmetric free-flight space launcher which approximates the shape of the main stage of the Ariane 5 shown in Fig. 2. The setup is based on the geometry in Statnikov et al.[29] where a classic conical nozzle was considered. The launcher model is composed of a Ariane-5 like main body with a reference thickness of D and a length of $5.6\,D$ and a nozzle fairing with a length of $0.85\,D$ and a thickness of $0.56\,D$ including the engine which is mounted downstream of the main body. The length of the fairing is defined such that an impingement of the shed shear layer shortly upstream of the end of the nozzle occurs which is the most critical condition since the pressure loads are largest around the impingement position. For the inner shape of the nozzle, a dual-bell geometry with a truncated ideal contour (TIC) for the base nozzle and a constant pressure nozzle extension with a design exit Mach number at altitude mode of $Ma_e = 3.3$ is used. The design transition nozzle pressure ratio of the dual-bell nozzle estimated by the method of characteristics combined with an empirical separation law is $NPR_{tr} = 12.6$. Note that compared to the setup used in Statnikov et al.[29] which serves as a reference case for the present investigation, the thickness of the nozzle extension is increased by $0.16\,D$ due to the particular characteristics of the dual-bell nozzle and the length of the nozzle extension is reduced by $0.55\,D$ to ensure an impingement of the shed shear layer close to the end of the nozzle.

Since the dynamic loads feature the highest nominal amplitudes during the transonic stage of the flight trajectory[5] , the simulation is performed at a freestream Mach number of $Ma_\infty = 0.8$. The freestream and nozzle flow conditions are summarized in Tab. 1. They are based on a number of experimental investigations recently performed on a planar launcher at the Bundeswehr University Munich within the framework of the German Collaborative Research Center Transregio 40[2] .

2.2 Zonal RANS/LES flow solver

The time-resolved computations are performed using a zonal RANS/LES solver which is based on a finite-volume method. The computational domain is split into several zones, see Fig. 3. In the zones where the flow is attached, i.e., the flow around the forebody and inside the base nozzle, the RANS equations are solved. The wake flow characterized by the separated shear layer is determined by an LES.

DOI: 10.13009/EUCASS2019-300

The Navier-Stokes equations of a three-dimensional unsteady compressible fluid are discretized second-order accurate using a mixed centered/upwind advective upstream splitting method (AUSM) scheme for the Euler terms. The non-Euler terms are approximated by a second-order accurate centered scheme. For the temporal integration an explicit 5-stage Runge-Kutta method of second-order accuracy is used. The monotone integrated LES (MILES) method determines the impact of the sub-grid scales. The solution of the RANS equations is based on the same discretization method. To close the time-averaged equations the one-equation turbulence model of Fares and Schröder[10] is used. For a comprehensive description of the flow solver see Statnikov et al.[27,30] .

The transition from the RANS to the LES domain is determined by the reformulated synthetic turbulence generation (RSTG) method developed by Roidl et al.[19,20] , which allows to reconstruct the turbulent fluctuations in the LES inlet plane based on the upstream RANS solution. This method generates turbulent fluctuations as a superposition of coherent structures and extends the idea of the synthetic eddy method (SEM) by Jarrin et al.[12] . The turbulent structures are generated at the inlet plane by superimposing virtual eddy cores, which are defined at random positions $\boldsymbol{x}_i$ in a virtual volume V_{virt}. This volume encloses the inlet plane and exhibits the dimension of the turbulent length scale l_x, the boundary-layer thickness at the inlet δ_0, and the width of the computational domain L_z in the streamwise, the wall-normal, and the circumferential direction. To take the inhomogeneity of the turbulent scales in the wall-normal direction into account, the virtual eddy cores are described by different shape factors and length and time scales depending on the wall-normal distance. Having N synthetic eddies, the normalized stochastic velocity fluctuations u'_m at the LES inlet plane are determined by the sum of the contribution $u^i_m(\boldsymbol{x}, t)$ of each eddy core i

$$u'_m(\boldsymbol{x}, t) = \frac{1}{\sqrt{N}} \sum_{i=1}^{N} \underbrace{\epsilon_i \, f^i_{\sigma,m}(\boldsymbol{x} - \boldsymbol{x}_i)}_{u^i_m(\boldsymbol{x},t)} , \tag{1}$$

where ϵ_i is a random number within the interval $[-1, 1]$, $f^i_{\sigma,m}$ is the shape function of the respective eddy, and the subscript m denotes the Cartesian coordinates in the streamwise, the wall-normal, and the spanwise direction. The final velocity components at the LES inflow plane u_m are composed of an averaged velocity component $u_{RANS,m}$ from the RANS solution and the normalized velocity fluctuations u'_m which are subjected to a Cholesky decomposition A_{mn} to assign the values of the target Reynolds-stress tensor $R_{mn} = A^T_{mn} A_{mn}$ corresponding to the turbulent eddy viscosity of the upstream RANS

$$u_m(\boldsymbol{x}, t) = u_{RANS,m} + A_{mn} \, u'_m(\boldsymbol{x}, t) \ . \tag{2}$$

To enable an upstream information exchange, i.e., a full bidirectional coupling of the LES and RANS zones, the time-averaged static pressure of the LES zone is imposed after a transition of three boundary-layer thicknesses at the end of the overlapping zone onto the RANS outflow boundary. The temporal window width used to compute the pressure for the RANS outflow plane is chosen such that high frequency oscillations of the LES pressure field are filtered out. A more detailed description of the zonal RANS/LES method specifying the shape functions and length scales is given in Roidl et al. [19,20] .

2.3 Computational mesh

In the zonal approach, the computational domain is divided into a RANS part enclosing the attached flow around the forebody and inside the base nozzle and an LES grid for the wake shown in Fig. 3. The RANS domain around the forebody extends to approximately 10D in the wall-normal direction and ends at $x/D = -0.05$ just upstream of the trailing edge of the main body located at $x/D = 0$. The LES section extends in the streamwise direction from $x/D = -0.5$ to $x/D = 10$ and in the radial direction, like the RANS mesh from $r/D = 0$ to $r/D = 10$. To ensure a fully developed boundary layer a transition length of approximately three boundary-layer thicknesses is required by the RSTG approach. Since the boundary-layer thickness directly upstream of the base shoulder is $\delta = 0.15D$, the LES inflow plane is positioned at $x/D = -0.5$ to guarantee a fully developed turbulent boundary layer upstream of the base shoulder. The LES inflow plane inside the nozzle is located at $x/D = 0.35$.

Table 1: Freestream and nozzle flow conditions.

	M	Re_D	U [m/s]	p_0 [Pa]	p [Pa]	NPR	T_0 [K]	T [K]
Freestream (∞)	0.8	$0.43 \cdot 10^6$	257	$1.2 \cdot 10^5$	$0.787 \cdot 10^5$		290	257
Nozzle exit	3.3		632	$7.87 \cdot 10^5$	$0.137 \cdot 10^5$	10	290	91

DOI: 10.13009/EUCASS2019-300

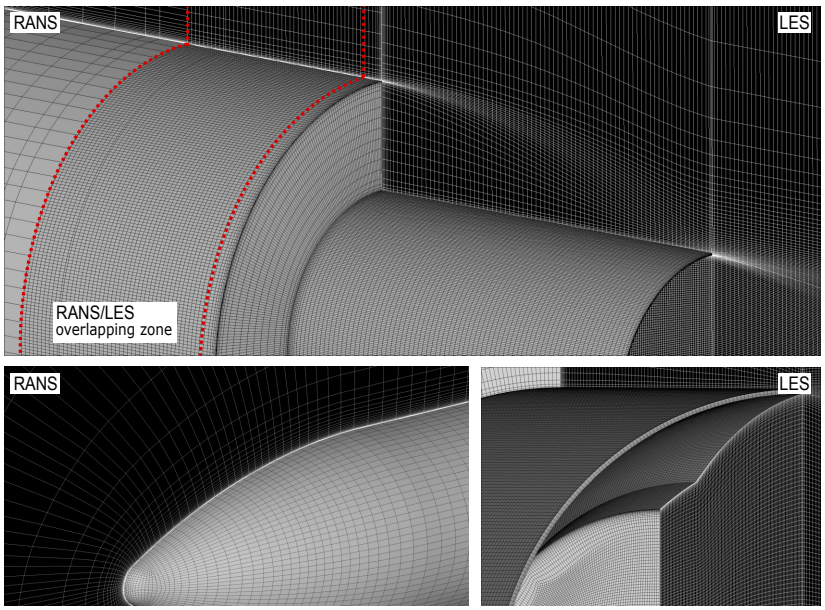

Figure 3: (a) Overview of the zonal grid topology; (b) zonal grid for the nozzle region; (c) LES grid for the wake zone.

The characteristic grid resolution in the area within the transition zone in inner wall units $l^+ = u_\tau/\nu$ is $\Delta x^+ = 50$, $\Delta r^+ = 2$, and $R\Delta\varphi^+ = 30$ for the LES zone and $\Delta x^+ = 350$, $\Delta r^+ = 1$, and $R\Delta\varphi^+ = 160$ for the RANS domain. The resolution is chosen according to typical mesh requirements in wall-bounded flows outlined by Choi and Moin[4] . In total, 590 million grid points are used for the zonal setup.

2.4 Dynamic mode decomposition

To separate large-scale coherent flow patterns from the turbulent background of the complex wake flow, modal decomposition (DMD) is applied in the present study. DMD is a data-driven decomposition techniques that in contrast to model-based approaches offer the advantage that no information about the underlying, mostly nonlinear and high-dimensional dynamical system is needed. Besides the identification of characteristic structures like large scale vortices being of particular importance to the underlying flow field, the extracted modes can serve as a basis for a reduced-order model, thus the original dynamical system can be projected onto a model system with fewer degrees of freedom. DMD is based on the Koopman operator to determine a basis of non-orthogonal spatial modes each associated with a specific constant frequency from a multi-dimensional data field obtained from time-resolved experiments or simulations. While modes of other modal decomposition techniques like, e.g., proper orthogonal decomposition (POD), exhibit a multi-frequency temporal content and are arranged according to their energy content, potentially missing dynamically highly relevant but low-energy modes, DMD provides single frequency modes which are assessed based on their dynamical importance. The DMD algorithm used in the present study was initially developed by Schmid[22] , including an economy-sized singular value decomposition (SVD) to guarantee a more robust calculation in case of an ill-conditioned input dataset. As usual for data-driven techniques, the DMD algorithm requires a sequence of equidistantly sampled snapshots arranged in form of the data matrix $\psi = \{\psi_0, \psi_1, \cdots, \psi_N\}$, where $\psi_n := \psi(x, y, z, t_n)$ represents the high-dimensional flow field at the discrete time step t_n. The DMD algorithm projects the data matrix onto a set of non-orthogonal spatial modes

$$\underbrace{[\psi_0\ \psi_1\ \ldots\ \psi_{N-1}]}_{\psi_0} \approx \underbrace{[\phi_1\ \phi_2\ \cdots\ \phi_N]}_{\Phi} \cdot \underbrace{\begin{pmatrix} a_1 & & & \\ & a_2 & & \\ & & \ddots & \\ & & & a_N \end{pmatrix}}_{D_a=diag\{a\}} \underbrace{\begin{pmatrix} 1 & \mu_1 & \cdots & \mu_1^{N-1} \\ 1 & \mu_2 & \cdots & \mu_2^{N-1} \\ 1 & \vdots & \ddots & \vdots \\ 1 & \mu_N & \cdots & \mu_N^{N-1} \end{pmatrix}}_{V_{and}} . \tag{3}$$

The quantity ϕ_n represents the spatial modes, a_n the amplitude of the corresponding DMD mode, and V_{and} the Vandermonde matrix containing the eigenvalues μ_n, which determine the temporal evolution, i.e., the frequencies and decay

DOI: 10.13009/EUCASS2019-300

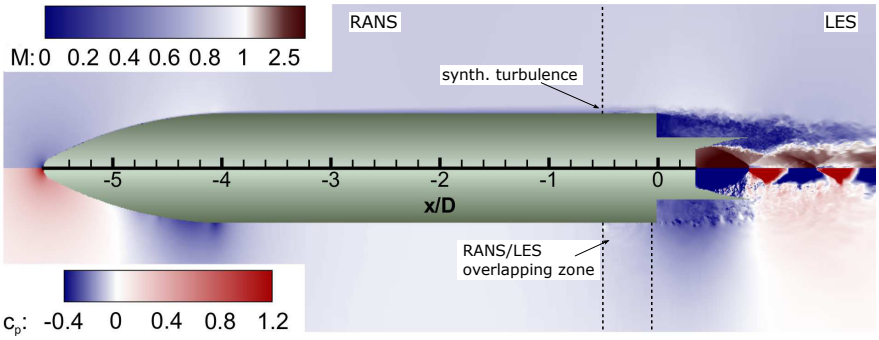

Figure 4: Flow topology of the generic axisymmetric space launcher configuration: Instantaneous Mach number distribution (top); pressure coefficient (bottom).

rates of the modes. To determine the unknown amplitudes a_n, the following convex optimization problem is solved

$$\underbrace{\text{minimize}}_{a} \; \|\boldsymbol{\psi}_0 - \Phi D_a V_{and}\|_F^2 \; . \tag{4}$$

This means that the amplitudes are chosen such that the entire input data sequence is optimally approximated. To reconstruct the temporally developing flow field the entire or a subset of the DMD modes can be superimposed according to the following equation

$$\psi(x, y, z, t) = \sum_{n=1}^{N} a_n e^{(\lambda_n t)} \phi_n(x, y, z) \; . \tag{5}$$

The quantity λ_n is the complex frequency which is determined by

$$\lambda_n = \frac{\log(\mu_n)}{\Delta t} = \underbrace{\frac{\ln|\mu_n|}{\Delta t}}_{D_n} + i \cdot \underbrace{\arctan\left(\frac{\mu_{n,imag}}{\mu_{n,real}}\right)\frac{1}{\Delta t}}_{\omega_n} \; , \tag{6}$$

where the real part D_n is the decay rate and the imaginary part ω_n is the angular frequency of the respective mode.

To select the DMD modes capturing the most important dynamic structures the sparsity-promoting algorithm introduced by Jovanovic et al.[13] is applied. Within the algorithm sparsity is induced by adding an additional term to the objective function in Eq. 4 that penalizes the l_1-norm of the vector of the DMD amplitudes. The following optimization problem is obtained

$$\underbrace{\text{minimize}}_{a} \; \|\boldsymbol{\psi}_0 - \Phi D_a V_{and}\|_F^2 + \gamma \sum_{i=1}^{N} |a_i| \; , \tag{7}$$

where the positive regularization parameter γ specifies the relative emphasis on the sparsity of the vector a. The quantity γ can be used to trade the approximation error with respect to the full data against the number of extracted modes.

The DMD algorithm is parallelized using MPI and ScaLAPACK to handle the large amount of data, the I/O is performed using the HDF5 parallel file format. For a more detailed description of the DMD algorithm, the reader is referred to Schmid[22] and Jovanovic et al.[13] .

3. Results

The discussion of the results is divided into three parts. First, the general characteristics of the wake flow topology plus dual-bell nozzle flow is presented and compared to the results of the previously investigated configuration with a classical conical nozzle. Subsequently, the dynamic behavior of the wake flow is investigated by classical statistical analysis, i.e. power spectral density and two-point correlation. Finally, DMD is applied to the wake flow to detect spatio-temporal modes which are responsible for the pressure loads on the outer nozzle surface.

3.1 Wake flow topology

The overall flow topology is visualized by the instantaneous distribution of the Mach number and the pressure coefficient around the generic space launcher shown in Fig. 4. The incoming freestream with a Mach number of $Ma_\infty = 0.8$

DOI: 10.13009/EUCASS2019-300

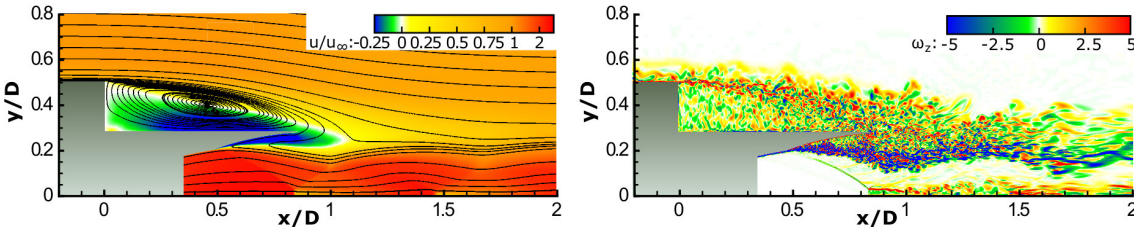

Figure 5: Flow topology: Time-averaged streamwise velocity contours and streamlines (left); instantaneous distribution of the spanwise vorticity component (right) at the azimuthal cut $\varphi = 0°$

accelerates along the launcher's nose to a local maximum of $Ma \approx 0.92$ and decelerates again to $Ma \approx 0.81$ around the main body. At the abrupt junction between the main body and the nozzle fairing, the incoming turbulent boundary layer separates and a turbulent free-shear layer emanates. Due to the low base pressure in the separation region, the flow accelerates towards the base shoulder. Inside the dual-bell nozzle, the flow accelerates to $Ma \approx 3$ and separates at the contour inflection forming classical shock cells. This is expected since the nozzle pressure ratio is below the transition pressure ratio.

Figure 5 shows the time-averaged streamwise velocity contours and streamlines and the instantaneous distribution of the spanwise vorticity component at an azimuthal cut $\varphi = 0°$. At the abrupt junction between the main body and the nozzle, the incoming turbulent boundary layer separates. The shed shear layer continuously broadens due to shear layer instabilities causing the initially small turbulent structures to grow in size and intensity similar to structures observed in the planar free-shear layers by Winant and Browand[31] . Further downstream, the structures either impinge on the surface approximately between $0.7 < x/D < 0.85$ or pass downstream without interacting with the nozzle surface. Downstream of the base, a large low pressure recirculation vortex occurs. In the dual-bell nozzle, the turbulent boundary layer separates at the contour inflection and shock cells are formed. In the nozzle extension, a backflow region forms entraining the eddies of the outer flow into the nozzle where they interact with the jet plume. Due to this interaction and the strong shear of the mean flow field between the backflow area and the jet, intensive turbulent structures are generated inside the nozzle extension. Due to the manifold of turbulent structures, a straightforward interpretation of the instantaneous flow field is quite complicated. Therefore, statistical analysis and DMD are used in the following sections to identify the underlying coherent motion of the wake dynamics leading to the buffet loads.

To investigate the influence of the new propulsion concept onto the pressure distribution along the launcher's surface, the wall-pressure coefficient c_p of the fully coupled RANS/LES simulation is shown as a function of the streamwise position for the dual-bell and conical nozzle configuration in Fig. 6 (a). Due to the local acceleration along the nose, the pressure initially drops to a local minimum of $c_p = -0.35$ and increases again as the flow decelerates along the forebody. On the first half of the nozzle extension at $0 < x/D < 0.5$, the pressure coefficient exhibits a slightly decreasing plateau-like minimum with a value around $c_p = -0.25$, followed by a quasi linear increase near the end of the nozzle which is caused by the impinging shear layer. The low base pressure exhibits a significant upstream influence on the attached boundary layer around the forebody. The flow accelerates already upstream of the shoulder leading to a decreasing pressure coefficient. This is taken into account in the simulation due to the full bidirectional coupling of the zonal method enabling an upstream propagation of the information from the LES to the RANS zone. The comparison between the two cases shows a qualitatively similar development of the wall pressure along the launcher's surface. The absolute pressure level in the recirculation region, however, is slightly decreased in the dual-bell nozzle configuration, which is due to the shorter nozzle length increasing the suction effect of the high streamwise momentum of the supersonic plume and a lower pressure level at the nozzle lip. The pressure increase

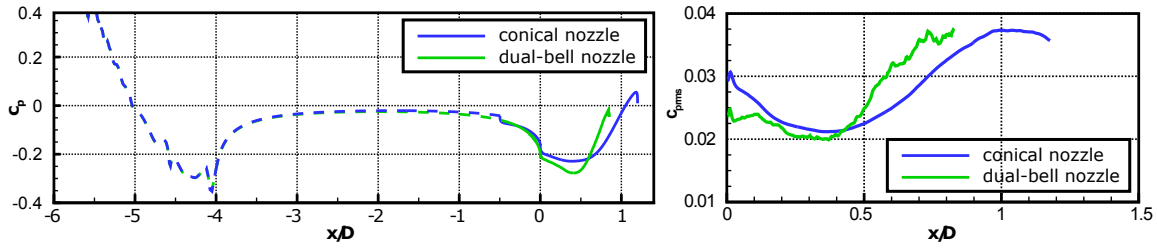

Figure 6: Streamwise distribution of the mean wall-pressure coefficient (left) and root-mean-square wall-pressure coefficient (right) along the outer nozzle fairing; comparison of the dual-bell nozzle and conical nozzle configurations.

DOI: 10.13009/EUCASS2019-300

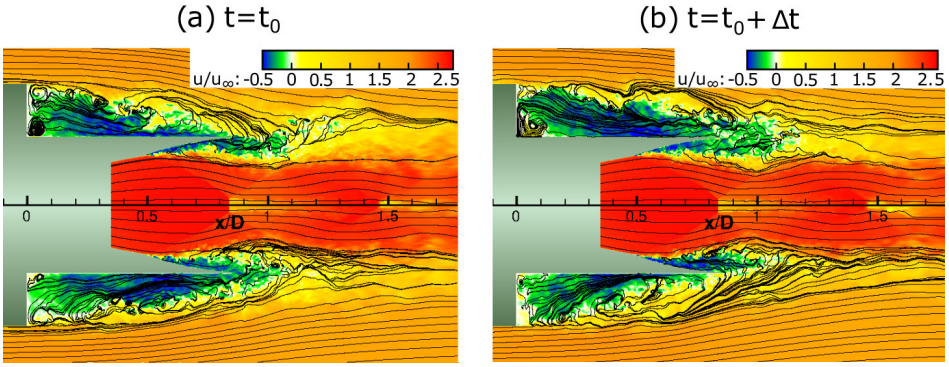

Figure 7: Instantaneous wake flow at two time steps: Streamwise velocity distribution and streamlines in the wake at an azimuthal cut $\varphi = 0°$ and $\varphi = 180°$.

towards the nozzle end is located further upstream in the dual-bell nozzle configuration since the shear layer impinges further upstream on the nozzle surface due to the smaller launcher's diameter.

The streamwise distribution of the root-mean-squre (rms) coefficient of the pressure fluctuations $c_{prms} = \overline{p'^2}/q_\infty$ on the outer nozzle surface is given for the two configurations in Fig. 6 (b). Both distributions exhibit a local enhanced pressure fluctuations level just downstream of the backward facing step at $x/D = 0.1$ which is caused by the secondary recirculation region. Further downstream, the rms values decrease before the fluctuations steadily increase in the streamwise direction, reach their maximum around the reattachment position, and slightly decrease toward the nozzle end. The increase in the pressure fluctuations around the reattachment position is generated by the vortical structures in the shear layer impinging on the nozzle surface. Note that the streamwise position, where the rms value starts to strongly increase, i.e., at $x/D \approx 0.4$ and $x/D \approx 0.6$, coincides with the location of the mean pressure recovery in Fig. 6 (a). While the overall distribution of the compared configurations is quite similar, the increase is located further upstream in the dual-bell case, since the step height and consequently the reattachment length is decreased. Since the maximum value at the end of the nozzle extension is comparable, the novel nozzle concept seems not to effect the dynamic loads onto the outer nozzle fairing.

The spanwise vorticity distribution in Fig. 5 (b) shows that the turbulent wake of the axisymmetric space launcher configuration is characterized by the interaction of a large number of structures exhibiting various time and length scales. The strong time dependence of the wake is also evident in the illustrations in Fig. 7 showing the instantaneous streamwise velocity distribution and streamlines at the azimuthal cut $\varphi = 0°$ and $\varphi = 180°$ at two time instants. At $t = t_0$ the recirculation region at the azimuthal cut $\varphi = 0°$ is relatively small leading to an impingement of the shear layer on the nozzle surface upstream of the time-averaged reattachment position. On the opposite side at $\varphi = 180°$, the recirculation region is greatly enlarged and the free-shear layer passes over the nozzle hardly interacting with it. Later at $t + \Delta t$, the dynamics is reversed, i.e., the recirculation region is enlarged at $\varphi = 0°$ and contracted at $\varphi = 180°$. This oscillation of the recirculation region and consequently, the variation of the impingement location are characteristic for planar separating-reattaching flow past backward facing steps[21,27] . They were also observed in the previous investigation of the axisymmetric configurations with a conical nozzle[29] . That is, the integration of the dual-bell nozzle does not seem to effect the overall dynamics of the flow around the nozzle fairing.

3.2 Analysis of the wake dynamics

3.2.1 Temporal spectral analysis

To evaluate the temporal periodicity of the wake dynamics and the resulting dynamic loads, the power spectral density (PSD) of the wall pressure fluctuations is discussed in the following. The PSD computation is based on a sequence of 3072 time instants equidistantly sampled with $\Delta t = 0.1 t_{ref}$ with $t_{ref} = D/u_\infty$. Welch's algorithm with Hanning windows of 512 samples each and an overlap of 50% is used. Hence, according to the Nyquist criterion frequencies in the range of $1.95 \cdot 10^{-2} < St_D < 5$ can be determined. To improve the statistical quality of the results, the PSD is computed for 1001 points equidistantly distributed in the circumferential direction and subsequently averaged in the frequency space.

The resulting premultiplied normalized PSD spectra at three streamwise positions are given in Fig. 8. At $x/D = 0.15$ the spectrum reveals two distinct peaks at $St_D \approx 0.04$ and $St_D \approx 0.2$, where St_D is the Strouhal number based on the launcher's diameter D and the freestream velocity u_∞. At the position further downstream, i.e., $x/D = 0.4$,

DOI: 10.13009/EUCASS2019-300

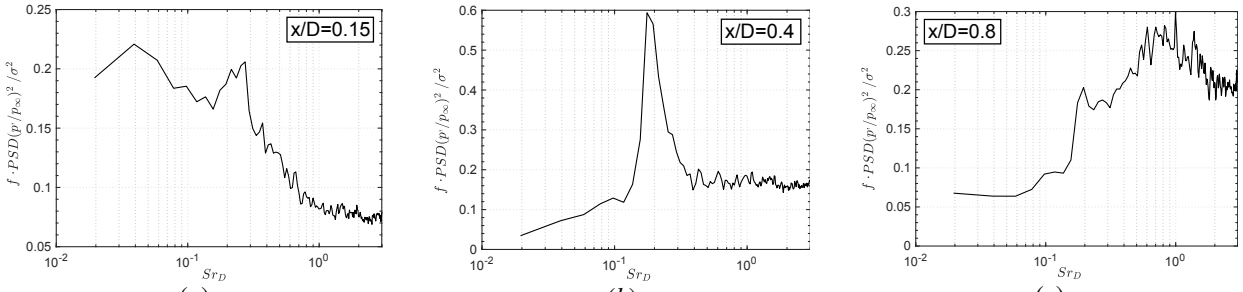

Figure 8: Premultiplied normalized power spectral density of the wall pressure fluctuations p'/p_∞ at $x/D = 0.15$ (a), $x/D = 0.4$ (b), and $x/D = 0.8$ (c).

the spectrum is dominated by a single peak at the buffet frequency, i.e., at $Sr_D \approx 0.2$ as known from the literature for similar space launcher configurations, e.g. Deck and Thorigny[6] , Schrijer et al.[24] , and Statnikov et al.[29] . At $x/D = 0.8$, just upstream of the end of the nozzle, the peak at $Sr_D \approx 0.2$ is also apparent. In addition, a broadband range at higher frequencies with a maximum at $Sr_D \approx 0.9$ resulting from the vortical structures within the separated shear layer impinging on the nozzle surface is visible. To sum up, the pressure spectrum at all three positions clearly shows a peak at the buffet frequency which is most pronounced around the center of the nozzle as known from the literature[6] .

To understand the underlying flow phenomena leading to the undesired pressure fluctuations, the azimuthal coherence of the pressure fluctuations and the resulting integrated buffet loads are subsequently analysed.

3.2.2 Two-point analysis

The spectral analysis in the previous section revealed two characteristic frequencies in the pressure fluctuations on the outer nozzle surface. To investigate the spatial coherence of these pressure fluctuations a two-point analysis is subsequently performed. The complex coherence function of two pressure sensors $p_1(x, \varphi_1, t)$ and $p_2(x, \varphi_2, t)$ located on a circumferential circle on the outer nozzle fairing is given by

$$C\left(f, x, \Delta\varphi\right) = \frac{G_{12}\left(f, x, \Delta\varphi\right)}{\sqrt{G_1\left(f, x, \varphi_1\right) G_2\left(f, x, \varphi_2\right)}} = C_r + iC_i \tag{8}$$

where G_{12} is the complex two-point cross power spectral density between p_1 and p_2, G_1 and G_2 the power spectral density of p_1 and p_2 and $\Delta\varphi = \varphi_1 - \varphi_2$. If we assume a homogeneous flow field without any mean swirl, C_i is zero and

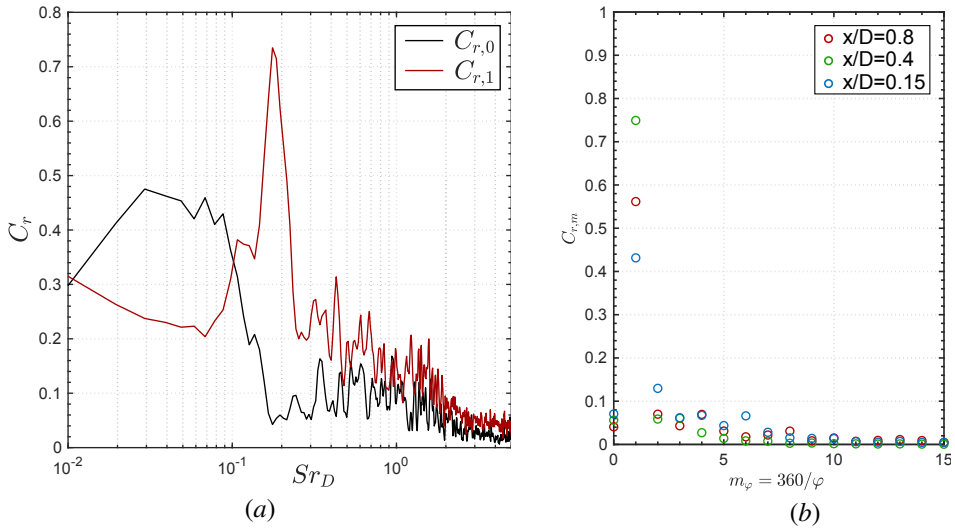

Figure 9: (a) Spectra of the first two azimuthal pressure mode coefficients $C_{r,0}, C_{r,1}$ at $x/D = 0.4$; (b) azimuthal pressure mode coefficients at the buffet frequency $Sr_D \approx 0.2$ at $x/D = 0.15$, $x/D = 0.4$ and $x/D = 0.8$.

DOI: 10.13009/EUCASS2019-300

C_r is symmetric in $\Delta\varphi$, i.e., $G_{12}(-\Delta\varphi) = G_{12}(\Delta\varphi)$. In addition, due to the axisymmetric configuration the coherence function is periodic in the circumferential direction, i.e., $C_r(\Delta\varphi + n2\pi) = C_r(\Delta\varphi)$. Due to these conditions, the real part of the coherence function can be expressed by a Fourier transform in the azimuthal direction

$$C_r(f, \Delta\varphi) = \sum_{m=0}^{\infty} C_{r,m}(f) \cos(m\Delta\varphi) \quad . \tag{9}$$

Since $\sum_{m=0}^{\infty} C_{r,m} = 1$, the $C_{r,m}$ coefficient describes the percentage of the fluctuation energy contained in each azimuthal constituent m at a specific frequency f. It is worth mentioning that $C_{r,0}$ describes an in-phase and $C_{r,1}$ an anti-phase relation between two pressure probes opposing in the circumferential direction. Hence, the side loads originating from the buffet phenomenon are mainly captured by the C_1 coefficient.

The spectrum of the first two azimuthal coefficients $C_{r,0}, C_{r,1}$ is given at $x/D = 0.4$, i.e., in the center of the recirculation region, in Fig. 9 (a). The spectrum of the axisymmetric mode $C_{r,0}$ shows a low frequency broadband content around $Sr_D \approx 0.04$ and decreasing values with higher frequency. The antisymmetric mode $C_{r,1}$ exhibits a distinct peak at the buffet frequency, i.e., $Sr_D \approx 0.2$ with an amplitude of 0.75, showing that 75% of the total pressure fluctuations at the specific frequency $Sr_D \approx 0.2$ are caused by this antisymmetric mode. In Fig. 9 (b) the azimuthal coefficients at the buffet frequency $Sr_D \approx 0.2$ are given for three different streamwise position. The Figure shows that along the whole outer nozzle surface the pressure fluctuations at the buffet frequency are dominated by the antisymmetric mode $C_{r,1}$ causing $44 - 75\%$ of the pressure fluctuations depending on the streamwise position while the remaining modes contribute only a small part to the pressure fluctuations. The results reveal that the buffet phenomenon and the resulting loads are caused by an antisymmetric flow event.

3.3 Buffet loads

To investigate the side loads arising from the periodic pressure oscillations outlined in the previous section, the instantaneous pressure fluctuations are integrated over the nozzle surface. Note that the side loads arising from the azimuthal component of the skin friction are neglected due to their considerably smaller amount compared to the pressure loads. The instantaneous side load coefficients for all time steps are shown in a polar plot in Fig. 10 (a), with $C_{FY}(t)$ and $C_{FZ}(t)$ denoting the Cartesian component of the integrate pressure loads normalized with the dynamic pressure $q_\infty = \frac{\gamma}{2} Ma^2 p_\infty$ and the main body cross section area $A = \frac{\pi D^2}{4}$. The image reveals that for the whole computational time span the orientation of the side load vector is random and isotropic which is in accordance with the axisymmetric geometry and inflow conditions. However, if we focus on the path of the side loads for a smaller time span matching an oscillation with the characteristic buffet frequency, i.e, $T(Sr_D \approx 0.2) = 5D/u_\infty$ given in Fig. 10 (b) for two time segments, it is evident that the side loads oscillate in an elliptical form that changes its azimuthal orientation arbitrarily in time. Thus, the results confirm the findings of the two-point analysis that an antisymmetric mode is responsible for the buffet loads. The findings coincide with the results of the reference configuration[29] with a conical nozzle showing that the impact of the dual-bell nozzle onto the wake flow is insignificant.

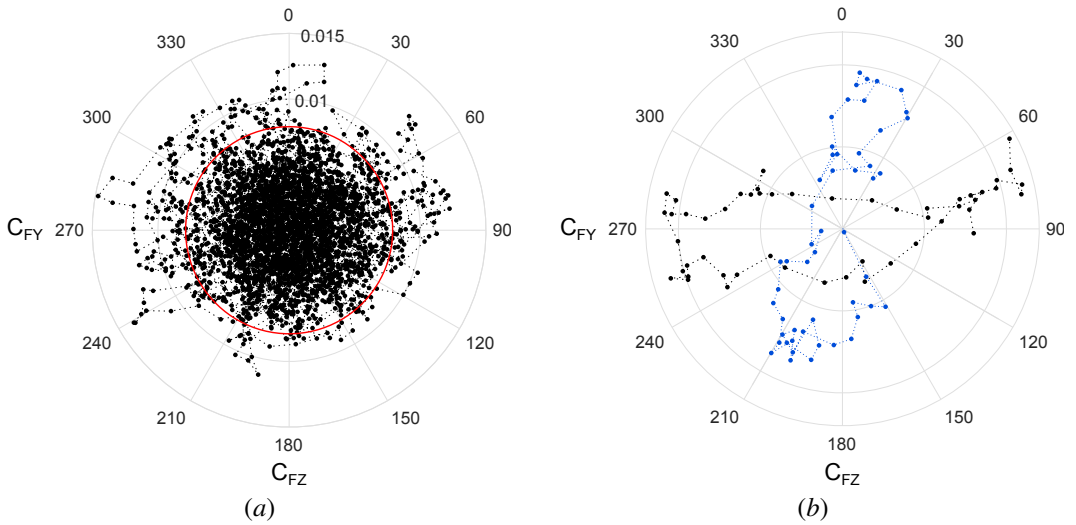

Figure 10: Scatter plot of the instantaneous side load onto the nozzle surface in polar coordinates: (a) Total simulation time; (b) two characteristic time intervals $T = 5D/u_\infty$

DOI: 10.13009/EUCASS2019-300

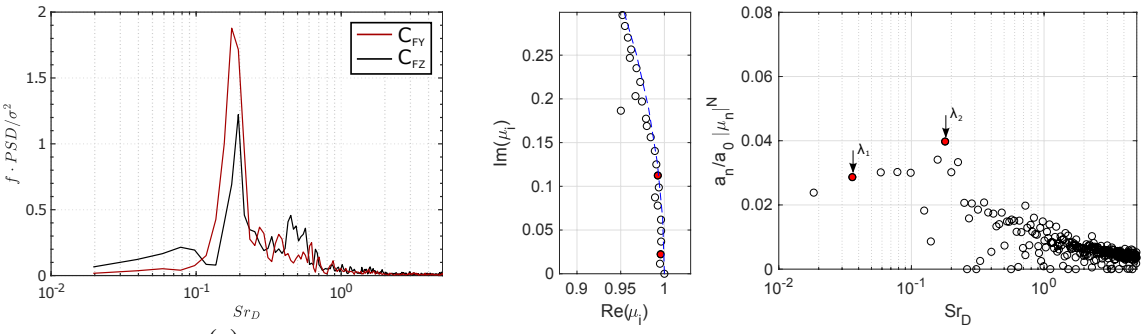

(a) (b)

Figure 11: (a) Premultiplied normalized power spectral density of the side load components; (b) normalized DMD spectrum of the three-dimensional velocity and pressure field; eigenvalues $\mu_n = e^{(\lambda_n \Delta t)}$ (left), normalized amplitude distribution versus frequencies $\Im(\lambda_n)$ (right).

The normalized frequency-premultiplied PSD for the two cartesian components of the buffet loads is given in Fig. 11 (a). The dominant peak at the buffet frequency, i.e., $S r_D \approx 0.2$ is clearly visible, containing most of the energy of the fluctuating force. Notice that the frequency perfectly coincide with the peak detected in the pressure fluctuations and the results reported in the literature[29] . The two characteristic frequency bands around $S r_D \approx 0.04$ and $S r_D \approx 0.9$ in the pressure spectrum are not visible in the PSD of the side loads indicating that the pressure loads at these frequencies do not feature an antisymmetric azimuthal shape.

To understand the origin of the buffet loads and to further investigate the impact of the dual-bell nozzle onto the wake flow, a dynamic mode decomposition of the wake flow is performed to extract dominant spatio-temporal modes from the time resolved three-dimensional flow field and to reduce the complex flow physics to a few degrees of freedom.

3.3.1 Modal analysis

The dynamic mode decomposition is performed using $N = 512$ samples of the three-dimensional velocity and pressure field of the wake. The samples are equidistantly distributed in time with $\Delta t = 0.1 t_{ref}$. To save computational costs, the spatial resolution is reduced by using only every second point in the streamwise and every fourth point in the radial and azimuthal direction. The resulting DMD spectrum is shown in Fig. 11 (b). The complex DMD eigenvalues μ_n are plotted together with the unit circle to enable the assessment of the decay rates. The amplitudes a_n of the DMD modes normalized by the amplitude a_0 of the mean mode and multiplied by the respective damping $|\mu_n|^N$ are shown as a function of their dimensionless frequency $S r_D = Im(\lambda_n) / (2\pi\Delta t)$. The multiplication by the damping factor reduces the amplitudes of transient modes which immediately decay and consequently, they are of minor importance for the overall flow dynamics. The selection of the important modes is based on the sparsity-promoting approach by Jovanovic et al.[13] . The two most stable modes of interest, i.e., $S r_{D,1}(\lambda_1) \approx 0.04$, $S r_{D,2}(\lambda_2) \approx 0.2$ are identified and marked by red filled circles. The dimensionless frequencies of these modes coincide with the characteristic frequencies of the PSD spectra of the pressure fluctuations shown in Fig. 8.

To visualize the three-dimensional shape and temporal evolution of the identified DMD modes, the spatial modes ϕ_n are superimposed with the mean mode ϕ_0 and reconstructed in time according to Eq. 5. The resulting three-dimensional velocity fields are given for the detected two modes at the time instance t_0 and after one half of the respective period time at $t_0 + 0.5T(\lambda_n)$ in Fig. 12. The flow is visualized by an iso-contour at a streamwise velocity of $u/u_\infty = 0.15$ and contours of streamwise velocity at the azimuthal cut $\varphi = 0°$ and $\varphi = 180°$.

The low frequency mode ϕ_1 describes a periodic pumping motion leading to an enlargement and contraction of the main recirculation vortex in the streamwise direction. The mode features a pronounced antisymmetry in the circumferential direction leading to an inverse oscillating motion at two opposite sides of the nozzle. The first mode captures the dynamic behavior of the recirculation bubble previously observed in Fig. 8. A similar spatio-temporal mode was found in a previous investigation of the configuration with a conical nozzle (Statnikov et al.[29]) and denoted as longitudinal cross-pumping mode. The second DMD mode at the buffet frequency $S r_{D,2}(\lambda_2) \approx 0.2$ describes a pronounced antisymmetric wave-like undulating motion of the shear layer. An analogous so called cross flapping motion was observed in the previous investigation by Statnikov et al.[29] and associated with an antisymmetric vortex shedding.

To investigate if the wave-like motion of the second mode is caused by a similar vortex shedding, the recon-

DOI: 10.13009/EUCASS2019-300

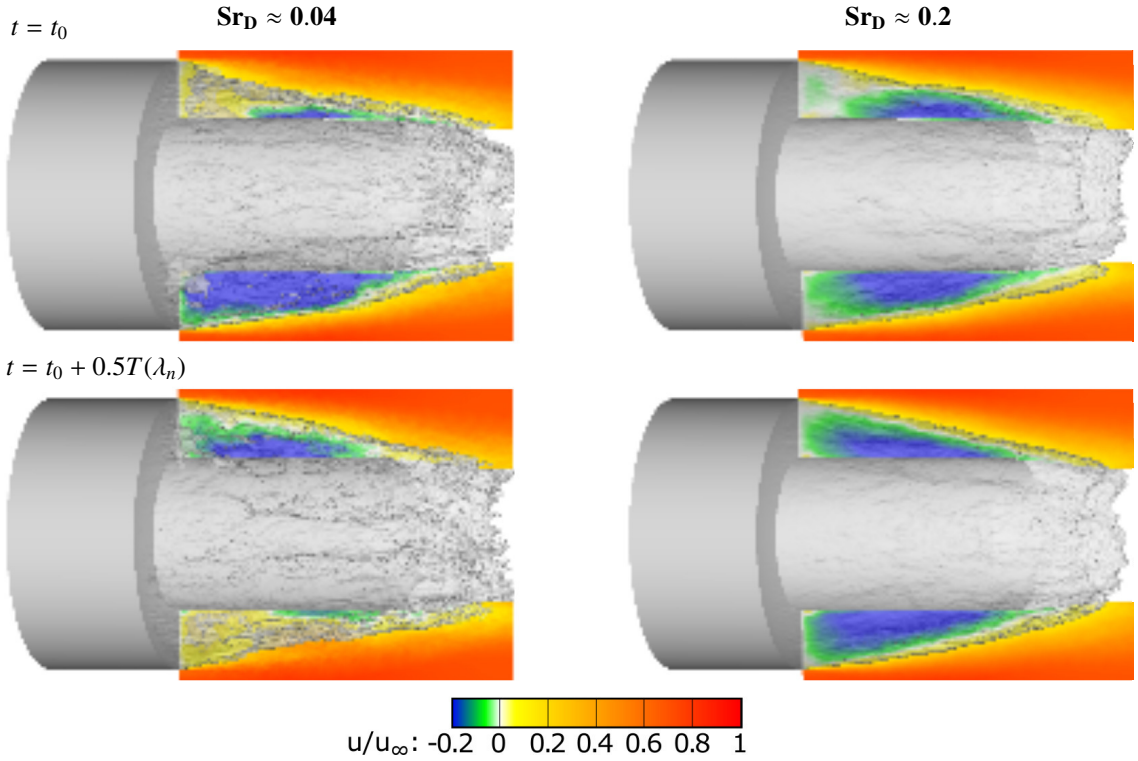

Figure 12: Reconstruction of the three-dimensional velocity field for the DMD mode at $S\,r_D \approx 0.04$ (left) and $S\,r_D \approx 0.2$ (right) at t_0 and after one half of the respective period time at $t_0 + 0.5T(\lambda_n)$

structed three-dimensional fluctuating pressure field is illustrated by pressure contours in Fig. 13 for the second DMD mode at the time instance t_0 and after one quarter of the time period, i.e. at $t_0 + 0.25T\ (\lambda_2)$. The temporal evolution of the mode exhibits the buffet phenomenon. That is, the pronounced periodic side loads are caused by large scale coherent regions with antisymmetric positive and negative pressure values propagating downstream from the base shoulder towards the nozzle lip. Since shear flows are characterized by pressure minima at the vortex center and pressure maxima at the stagnation point between two adjacent vortices, the pressure field proves that the cross flapping motion is caused by an antisymmetric vortex shedding.

In summary, the modal decomposition of the wake flow indicates that the dynamic behavior of the wake and consequently, the buffet loads acting on the outer nozzle fairing are caused by a cross flapping motion of the shear layer. The detected modes are similar to the modes of the reference configuration with the conventional conical nozzle[29] showing that in the current parameter range and operation mode the dynamics of the recirculation bubble downstream of the base shoulder is not affected by the dual-bell nozzle.

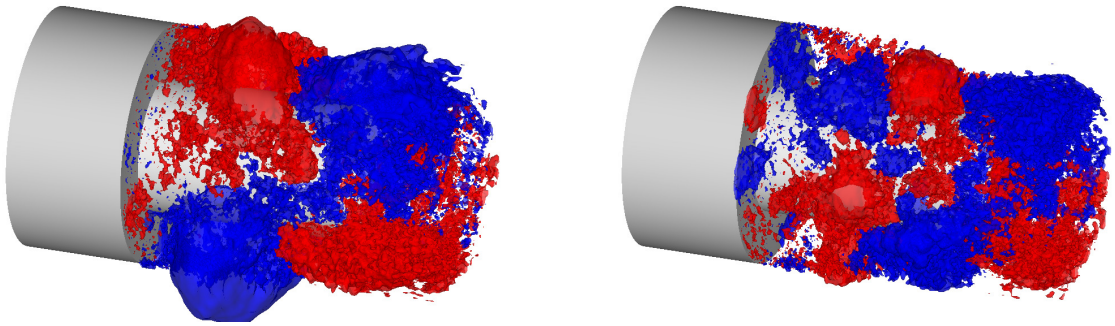

$t = t_0$ $\qquad$ $t = t_0 + 0.25T(\lambda_2)$

Figure 13: Reconstruction of the fluctuating three-dimensional pressure field of the antisymmetric mode at $S\,r_D \approx 0.2$ visualized by two pressure iso-surfaces with positive and negative values at the time instance t_0 and after one quarter of the time period $(t_0 + 0.25T(\lambda_2)$.

DOI: 10.13009/EUCASS2019-300

4. Conclusions

The turbulent wake of a generic axisymmetric space launcher equipped with a dual-bell nozzle is numerically investigated to determine the influence of the advanced propulsion concept onto the intricate wake flow. The investigation is performed in transonic freestream, i.e., $M_\infty = 0.8$ and $Re_D = 4.3 \cdot 10^5$, and the dual-bell nozzle is operated at sea-level condition, i.e., with a flow separation at the contour inflection. A zonal RANS/LES approach combined with a synthetic turbulence generation method is used for the simulations.

The wake of the axisymmetric space launcher is characterized by the shear layer separating at the shoulder of the main body and impinging on the nozzle. The streamwise extension of the resulting recirculation region strongly varies in time, exhibiting an antisymmetric behavior in the circumferential direction. The comparison with a conventional TOP nozzle reveals that the overall flow topology downstream of the base shoulder is hardly affected by the modified nozzle contour. However, the shock and flow separation originating from the nozzle contour inflection and the consequential entrainment of the outer flow into the nozzle cause enhanced fluctuations in the nozzle.

Using a temporal Fourier transform of the wall pressure fluctuations on the outer nozzle fairing a dominant characteristic frequency at $St_D \approx 0.2$ matching the buffet frequency known from the literature is detected. In addition, a distinct low frequency peak at $St_D \approx 0.04$ near the base and a broadband higher frequency range around $St_D = 0.9$ caused by the impinging shear layer is observed. It is shown by a two-point correlation analysis that the wake flow is dominated by an antisymmetric mode that is responsible for about 75% of the pressure fluctuations at the buffet frequency. The modal analysis of the wake flow based on DMD reveals that the dynamic buffet loads at $St_D \approx 0.2$ are caused by an oscillating wavy motion of the shear layer that is triggered by an antisymmetric vortex shedding. A second low frequency DMD mode at $St_D \approx 0.04$ describes an antisymmetric oscillating growth and shrinkage of the main recirculation vortex explaining the dynamic behavior observed in the instantaneous streamline snapshots and the low frequency pressure fluctuations on the nozzle wall. The presented dual-bell nozzle configuration exhibits a similar flow topology and wake dynamics compared to the reference configuration with a classical conical nozzle. Therefore, it is stated that for the present flow condition the wake downstream of the base shoulder is not affected by the dual-bell nozzle concept.

5. Acknowledgments

Financial support has been provided by the German Research Foundation (Deutsche Forschungsgemeinschaft - DFG) in the framework of the Sonderforschungsbereich Transregio 40. The authors are grateful for the computing resources provided by the High Performance Computing Center Stuttgart (HLRS) and the Jülich Supercomputing Center (JSC) within a Large-Scale Project of the Gauss Center for Supercomputing (GCS).

References

[1] I. Bolgar, S. Scharnowski, and C. J. Kähler. The effect of the mach number on a turbulent backward-facing step flow. *Flow Turbulence Combust*, 101(3):653–680, 2018.

[2] I. Bolgar, S. Scharnowski, and C. J. Kähler. Experimental analysis of the interaction between a dual-bell nozzle with an external flow field aft of a backward-facing step. *21. DGLR-Fach-Symposium der STAB*, 2018.

[3] P. Bradshaw and F.Y.F. Wong. The reattachment and relaxation of a turbulent shear layer. *J. Fluid Mech.*, 52(1):113–135, 1972.

[4] H. Choi and P. Moin. Grid-point requirements for large eddy simulation: Champan's estimates revisited. *Physics of Fluids*, 24(011702), 2012.

[5] S. David and S. Radulovic. Prediction of buffet loads on the Ariane 5 afterbody. *6th International Symposium on Launcher Technologies, Munich, Germany, 8-11 November*, 2005.

[6] S. Deck and P. Thorigny. Unsteadiness of an axisymmetric separating-reattaching flow: Numerical investigation. *Physics of Fluids*, 19(065103), 2007.

[7] D. Deprés, P. Reijasse, and J. P. Dussauge. Analysis of unsteadiness in afterbody transonic flows. *AIAA J.*, 42(12):2541–2550, 2004.

[8] D. M. Driver, H. L. Seegmiller, and J. G. Marvin. Time-dependent behavior of a reattaching shear layer. *AIAA J.*, 25(7):914–919, 1987.

DOI: 10.13009/EUCASS2019-300

[9] J. K. Eaton and J. P. Johnston. A review of research on subsonic turbulent flow reattachment. *AIAA J.*, 19(9):1093–1100, 1981.

[10] E. Fares and W. Schröder. A general one-equation turbulence model for free shear and wall-bounded flows. *Flow Turbul. Combust.*, 73:187–215, 2004.

[11] R. Friedrich and M. Arnal. Analysing turbulent backward-facing step flow with the low-pass-filtered Navier-Stokes Equations. *Journal of Wind Engineering and Industrial Aerodynamics*, 35:101–128, 1990.

[12] N. Jarrin, S. Benhamadouche, D. Laurence, and R. Prosser. A synthetic-eddy-method for generating inflow conditions for large-eddy simulations. *Int. J. Heat Fluid Flow*, 27:585–593, 2006.

[13] M. R. Jovanovic, P. J. Schmid, and J. W. Nichols. Sparsity-promoting dynamic mode decomposition. *Physics of Fluids*, 26(024103), 2014.

[14] H. Le, P. Moin, and J. Kim. Direct numerical simulation of turbulent flow over a backward-facing step. *J. Fluid Mech.*, 330:349–374, 1997.

[15] I. Lee and H. J. Sung. Characteristics of wall pressure fluctuations in separated and reattaching flows over a backward-facing step: Part I. Time-mean statistics and cross-spectral analyses. *Experiments in Fluids*, 30:262–272, 2001.

[16] S. Loosen, M. Meinke, and W. Schröder. Numerical investigation of jet-wake interaction for a dual-bell nozzle. *12th International ERCOFTAC Symposium on Engineering Turbulence Modelling and Measurements, Montpellier, France*, 2018.

[17] E. Martelli, F. Nasuti, and M. Onofri. Numerical parametric analysis of dual-bell nozzle flows. *AIAA Journal*, 45(3), 2007.

[18] D. Proshchanka, Y. Koichi, H.Tsukuda, K. Araki, Y. Tsujimoto, T. Kimura, and K. Yokota. Jet oscillation at low-altitude operation mode in dual-bell nozzle jet oscillation at low-altitude operation mode in dual-bell nozzle jet oscillation at low-altitude operation mode in dual-bell nozzle. *J. Propuls. Power*, 28(5):1071–1080, 2012.

[19] B. Roidl, M. Meinke, and W. Schröder. A reformulated synthetic turbulence generation method for a zonal RANS-LES method and its application to zero-pressure gradient boundary layers. *Int. J. Heat Fluid Flow*, 44:28–40, 2013.

[20] B. Roidl, M. Meinke, and W. Schröder. Boundary layers affected by different pressure gradients investigated computationally by a zonal RANS-LES method. *Int. J. Heat Fluid Flow*, 45:1–13, 2014.

[21] Sven Scharnowski, Istvan Bolgar, and Christian J. Kähler. Characterization of turbulent structures in a transonic backward-facing step flow. *Flow, Turbulence and Combustion*, pages 1–21, 2016.

[22] P. J. Schmid. Dynamic mode decomposition of numerical and experimental data. *J. Fluid Mech.*, 656:5–28, 2010.

[23] D. Schneider and C. Génin. Numerical investigation of flow transition behavior in cold flow dual-bell rocket nozzles. *J. Propuls. Power*, 32(5):1212–1219, 2016.

[24] F. Schrijer, A. Sciacchitano, and F. Scarano. Spatio-temporal and modal analysis of unsteady fluctuations in a high-subsonic base flow. *Physics of Fluids*, 26(086101), 2014.

[25] A. Silveria Neto, D. Grand, O. Metais, and M. Lesieur. A numerical investigation of the coherent vortices in turbulence behind a backward-facing step. *J. Fluid Mech.*, 256:1–25, 1993.

[26] R. Stark and C. Génin. Sea-level transitioning dual bell nozzles. *CEAS Space J.*, 9:279–287, 2017.

[27] V. Statnikov, I. Bolgar, S. Scharnowski, M. Meinke, C. J. Kähler, and W. Schröder. Analysis of characteristic wake flow modes on a generic transonic backward-facing step configuration. *Europ. J. Mech. B/Fluids*, 59:124–134, 2016.

[28] V. Statnikov, M. Meinke, and W. Schröder. Analysis of spatio-temporal wake modes of space launchers at transonic flow. *AIAA Paper*, 2016-1116, 2016.

[29] V. Statnikov, M. Meinke, and W. Schröder. Reduced-order analysis of buffet flow of space launchers. *J. Fluid Mech.*, 815:1–25, 2017.

DOI: 10.13009/EUCASS2019-300

[30] V. Statnikov, T. Sayadi, M. Meinke, P. Schmid, and W. Schröder. Analysis of pressure perturbation sources on a generic space launcher after-body in supersonic flow using zonal turbulence modeling and dynamic mode decomposition. *Physics of Fluids*, 27(016103), 2015.

[31] C. D. Winant and F. K. Browand. Vortex pairing: The mechanism of turbulent mixing-layer growth at moderate reynolds number. *J. Fluid Mech.*, 63(2):237–255, 1974.